

Toward Autonomous Robotic Micro-Suturing using Optical Coherence Tomography Calibration and Path Planning

Yuan Tian, Mark Draelos, PhD, Gao Tang, Ruobing Qian,
Anthony Kuo, MD, Joseph Izatt, PhD, Kris Hauser, PhD

Abstract—Robotic automation has the potential to assist human surgeons in performing suturing tasks in microsurgery, and in order to do so a robot must be able to guide a needle with sub-millimeter precision through soft tissue. This paper presents a robotic suturing system that uses 3D optical coherence tomography (OCT) system for imaging feedback. Calibration of the robot-OCT and robot-needle transforms, wound detection, keypoint identification, and path planning are all performed automatically. The calibration method handles pose uncertainty when the needle is grasped using a variant of iterative closest points. The path planner uses the identified wound shape to calculate needle entry and exit points to yield an evenly-matched wound shape after closure. Experiments on tissue phantoms and animal tissue demonstrate that the system can pass a suture needle through wounds with 0.27 mm overall accuracy in achieving the planned entry and exit points.

I. INTRODUCTION

Suturing is a basic surgical skill used in microsurgery to repair wounds and severed blood vessels and nerves, but it is tedious, time-consuming, and requires substantial training [1]. Robotic assistance has been proposed for suturing in open surgery, laparoscopic surgery, and microsurgery, with teleoperated surgical systems increasing the surgeon’s dexterity, as well as autonomous techniques that can alleviate burden on the surgeon. Automation of suturing is still a challenging task due to deformation of the tissue as the needle passes through it, the need for regrasping to complete multiple throws, and incorporation of imaging feedback to estimate wound shape and guide the needle successfully along planned paths. The needle is occluded as it passes through the tissue, and it is difficult to perform accurately 3D mapping of biological tissues with stereo vision techniques. The challenge is particularly acute in the microsurgery setting, since existing sensing and actuation technologies do not perform at the required level of precision needed to complete reliable suturing.

To plan a suturing path and achieve sub-millimeter suturing precision, we propose a needle calibration and insertion system with optical coherence tomography (OCT) imaging.

This work is partially supported by NIH Grant R21-EY029877.

Y. Tian is with the Department of Electrical and Computer Engineering, Duke University, Durham, NC, USA.

M. Draelos, R. Qian and J. Izatt are with the Department of Biomedical Engineering, Duke University, Durham, NC, USA.

G. Tang and K. Hauser are with the Department of Computer Science, University of Illinois Urbana-Champaign, Urbana, IL, USA.

A. Kuo is with the Department of Ophthalmology, Duke University Medical Center, Durham, NC, USA.

yuan.tian277@duke.edu

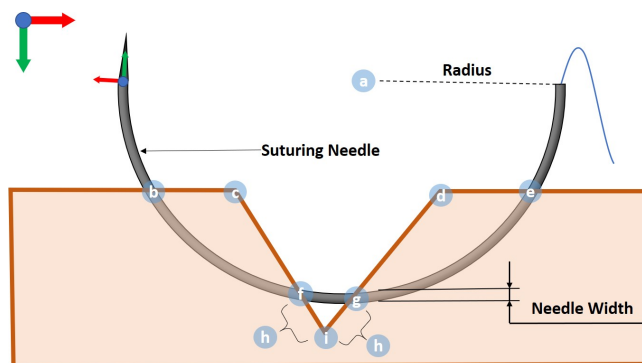


Fig. 1. Cross-sectional geometry of the incised wound and suturing path, showing a) suturing center, b) left exit point, c) wound start point, d) wound end point, e) right bite point, f) left bite point, g) right exit point, h) distance from the deepest point to the left bite point (set to be equal to the distance to the right exit point), i) wound deepest point.

OCT is a laser-based imaging technique that exploits interference to resolve the distance of reflectors along the beam’s path to within several micrometers [6]. By scanning the beam, a cross-sectional view (or B-scan) of the tissue is produced, and further sweeping the beam in a raster pattern yields a 3D volume (a $\sim 1 \text{ cm}^3$ cube in our system). Although OCT has deepest penetration in transparent tissues like those of the eye, it can also be used to image the surfaces and first millimeters of scattering tissues like skin. OCT has also been used to track tissues and surgical tools in eye surgery [10]. To guide the needle precisely, we perform calibration, perception, and planning in the OCT imaging frame. To calibrate the needle tip and robot with respect to the OCT frame, we use the observed needle surface voxels to simultaneously optimize the needle, robot, and OCT frames with a modified iterative closest points (ICP) [2] algorithm that emphasizes an accurate fit at the needle tip. A suturing path planner chooses a suturing path such that the two sides of the wound will match after closure, without dead space [4]. The top layer, wound keypoints, and suture path are calculated automatically from OCT data (Fig. 1).

Closed-loop imaging guidance is challenging due to significant artifacts including refraction and OCT shadowing by the needle driver. Instead, our experiments observe that open-loop execution of a circular suture path lead to high accuracy between the planned and actual needle entry and exit point, even under significant tissue deformation. A unique aspect of our experiments is that we use 3D OCT to image the resulting suture path after the needle is pulled through and

the tissue returns to a rest state. Experiments in a tissue phantom and porcine skin show the targeted entry and exit points are reached with RMSE of approximately 0.27 mm, which is less than the needle width.

II. RELATED WORK

Several researchers have studied the use of robots and imaging guidance for suturing and micromanipulation assistance. Using direct teleoperation, human surgeons are able to complete suturing for anastomoses of 3mm artificial blood vessels using the Intuitive Surgical DaVinci robot [1], but to our knowledge surgical robots have not yet been used for microsurgical suturing in vivo.

Autonomous suturing has been studied for at least two decades. Early work by Kang and Wen proposes a laparoscopic robot that can perform manually controlled or semi-autonomous motions for several tasks, including suturing and automatic knot tying [8]. Each motion is initiated by a surgeon. Staub et al present an image-based guidance system for improved accuracy in guiding a suturing needle to pierce the tissue at a surgeon-indicated spot, as directed by a laser pointer [14]. 3–10 mm errors were observed from their system. More recent work has addressed multi-throw suturing using a dual armed laparoscopic robot, using a special needle gripper that reduces grasp positioning errors and feedback from a stereo vision system [13]. Their calibration system obtains needle predictions with translational error of approximately 2.9mm, and completes 86% of throws. Our path planner is highly related to the method of Jackson and Cavusoglu for path planning of needles entering triangular shaped wounds [7]. The geometry of a circular needle entering a wound was analyzed, and we adopt many of the same conventions here. Their paths were executed on a DaVinci robot with a 12.7 mm radius needle. A similar approach was adopted by Pedram et al who studied the problem of needle selection for varying wound geometries [12]. The errors of their entry and exit points were greater than 4.5 mm with a 15 mm radius needle. Overall, accuracy must be improved significantly for autonomous suturing in microsurgery. Our system integrates the planner with imaging feedback, calibration, and analysis of errors in the suture path for a needle with 2 mm radius, obtaining $10\times$ better accuracy than previously reported results.

In the microsurgical domain, OCT-guided robots have been studied as a method for assisting surgeons to complete telemanipulated tasks, primarily in the eye. Yu et al present a B-mode OCT-integrated forceps tool for haptic-controlled microsurgery to assist in retinal membrane peeling [15]. Nasser et al present an OCT and robot guidance system to assist in precise injections for macular degeneration [11], and Draelos et al present a hand-guided robot that provides stabilization and OCT guidance in the cornea [3].

Our calibration process is highly related to the work of Zhou et al that presents an OCT-based needle tip tracking and calibration scheme [16]. This work identified pixels likely to belong to the needle from the OCT B-scans and segmented the needle from the background using a voting

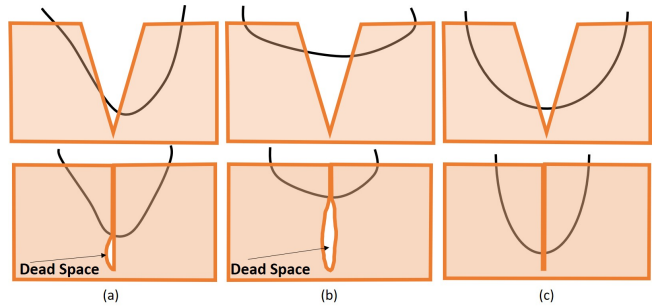


Fig. 2. (a) The left bite point is higher than the right exit point, so a dead space remains after closure. (b) The suturing depth is not sufficiently deep, which leaves a dead space after the wound is closed. (c) When the suturing path equalizes the wound sides and is sufficiently deep, then no dead space remains post-closure.

scheme. Calibrating the robot-OCT frame and tracking the needle led to an impressive $\approx 10\mu\text{m}$ error as the needle moved along an XYZ translation stage. They also extended their method to 6DOF tracking using ICP with similar levels of accuracy [17]. Our work differs in that we consider a curved needle grasped by a needle driver, which makes needle identification more difficult due to artifacts caused by shadowing, reflection artifacts, and mirror images from the complex conjugate of the needle driver. Furthermore, our calibration process accounts for regrasping errors rather than using a fixed needle mount.

III. METHODS

Our system is designed to calibrate a robot-mounted circular needle and automatically insert it through a wound, all using OCT imaging. To focus on the calibration and path planning problems, we show only the single-throw problem and leave multi-throw suturing for future work. Our method assumes that 1) the needle body is a circular arc; 2) the needle diameter is larger than the wound width, so that no significant travel is needed to bring the wound sides together; 3) the entire wound is within the robot and OCT workspaces; and 4) the patient anatomy permits needle insertion by rotation about an axis parallel to the wound.

Consider the plane of the needle and a cross sectional view of a wound, where the needle is passing from right to left. To close the wound, the needle passes through the right bite point, right exit point, left bite point, and the left exit point in sequence (Fig. 1). If the right exit point and left bite point are not well-aligned with the wound’s deepest point, the resulting dead space after wound closure (Fig. 2) promotes infection [4]. Our planner generates a suture path that avoids such dead space.

A. Error Analysis

The overall needle guidance error is influenced by many elements:

- *Needle grasping uncertainty* is introduced when the the needle driver grasps the needle.
- *Wound calculation errors* can be introduced during wound segmentation and keypoint identification.

- *Needle and OCT calibration error* remain after calibration, although needle grasping uncertainty is reduced.
- *Robot repeatability and accuracy* limits the overall system performance.
- *Tissue deformation* from friction as the needle passes through the tissue can be significant (Fig. 3).
- *Conjugate image* overlap in OCT can produce artifacts that cause errors in needle identification. We manually delete conjugate images to avoid this problem.

We mitigate these errors through calibration to significantly reduce the needle grasping uncertainty and surgeon supervision of wound analysis. Robot error is minimized with a repeatability of $10\ \mu\text{m}$. The overall error is thus dominated by residual calibration error and tissue deformation. Closed-loop corrections under OCT imaging feedback would further reduce this error, but mid-insertion images suffer from shadowing, needle specular reflections, and refraction through (Fig. 3).

B. Hardware

We use a custom OCT engine with a 100 kHz swept-source laser centered at 1060 nm (Axsun Technologies; Billerica, MA), an adjustable transmissive reference arm, and balanced detection. We configured this engine [3] to capture OCT volumes with sampling density $715 \times 800 \times 1327$ pixels and field of view $10 \times 10 \times 7.19$ mm. Our robot to perform the suturing needle insertion is a 6-joint IRB 120 Robot (ABB Robotics; Shanghai, China) with a specified repeatability of $10\ \mu\text{m}$.

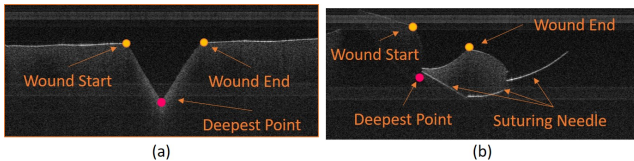


Fig. 3. (a) The wound shape before the needle insertion. (b) The wound shape after the needle insertion, undergoes significant deformation.

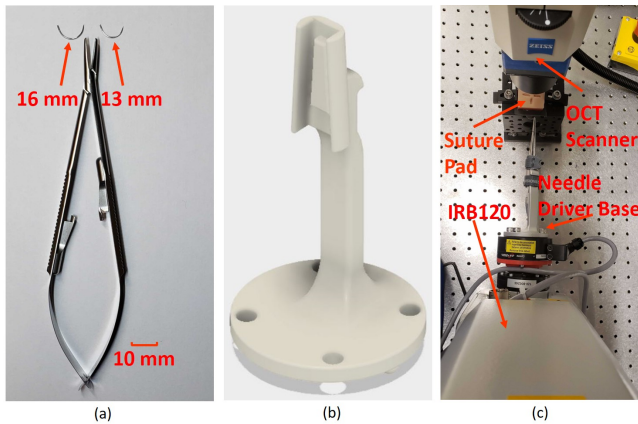


Fig. 4. (a) Needle driver and suturing needles used in our experiments. (b) Needle driver holder design. (c) Top-down view of the needle holder, robot, and OCT scanner with the suture pad tissue phantom. (best viewed in color)

We use a taper point, half-circle 5-0 suturing needle with 16 mm arc length for tissue phantom insertions. A taper point, half-circle 4-0 suturing needle with 13 mm arc length is used for porcine skin insertions. The needles' widths, as marked in Fig. 1 are 0.510 mm and 0.448 mm, respectively. The needle is grasped with a locking Castroviejo needle driver (Ambler Surgical; Exton, PA) which is mounted to the robot's end-effector with a custom holder. This holder keeps the grasped needle's rotation axis approximately coincident with the robot's last joint axis (Fig. 4). This minimizes robot wrist and elbow movement to avoid collision with the surgical field and patient.

C. Calibration

Our calibration procedure calculates the transformations from the world frame to the OCT frame and from the robot end-effector frame to the needle frame. We define the needle origin at the interface between the needle tip and the needle body which facilitates path planning. The needle tip's conical nature causes the body and tip to follow separate paths when rotated [7]. This misalignment may cause friction and deformation between the needle body and the suturing path.

1) *ICP Estimates of Needle Tip Transform*: To estimate the needle transform in the OCT frame, we use Iterative Closest Points [2] which aligns points in the OCT field (source point cloud) and the needle CAD model (target point cloud). We identify the needle points as a subset of the bright pixels in the OCT maximum intensity projection (MIP). Because of artifacts from highlights and mirror images of the needle driver, we select out only the points belonging to the needle in Open3D [18]. Standard ICP frequently mismatches the needle tip, however, because the point is dominated by body points (Fig. 5a). We overcome this problem by estimating tip points from an initial ICP fit and increasing their weight for a second ICP fit (5b). The second fit yield better alignment, especially at the needle tip.

2) *Calibration Algorithm*: Our calibration algorithm seeks to solve

$$T_{ICP}^{-1} = T_{OCT}^{-1} T_{EE} T_N, \quad (1)$$

where T_N is the needle frame in the end-effector frame, T_{OCT} is the OCT frame in the world, T_{EE} is the end-effector frame in the world from forward kinematics, and T_{ICP} is the ICP-derived transformation from the needle frame to the OCT frame. We guide the robot to m different poses, yielding paired observations T_{ICP_i} and T_{EE_i} , for $i = 1, \dots, m$. We minimize the error in Eq. 1 over T_N and T_{OCT} using a Levenberg-Marquardt method. These configurations should sample needle poses roughly uniformly across the OCT workspace and with a diversity of needle orientations. They should also be chosen so the needle tip's point cloud is visible and not shadowed by the body or needle driver. Our calibration set is a manually defined set of 9 poses.

D. Wound Analysis

Wound analysis processes an OCT B-scan image and produces the following shape information: the top layer, the start point, the end point and the deepest point. We begin by

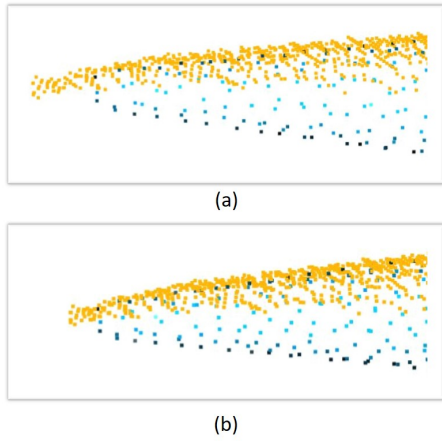


Fig. 5. The yellow point clouds are the source point clouds captured in the OCT system, and the blue point clouds are target point clouds built in the CAD software. (a) Original ICP result. We transfer the source point cloud to the target point cloud frame. The needle tip of these 2 point clouds has mismatching. (b) The modified ICP result. The mismatching of the 2 point clouds has been alleviated. (best viewed in color)

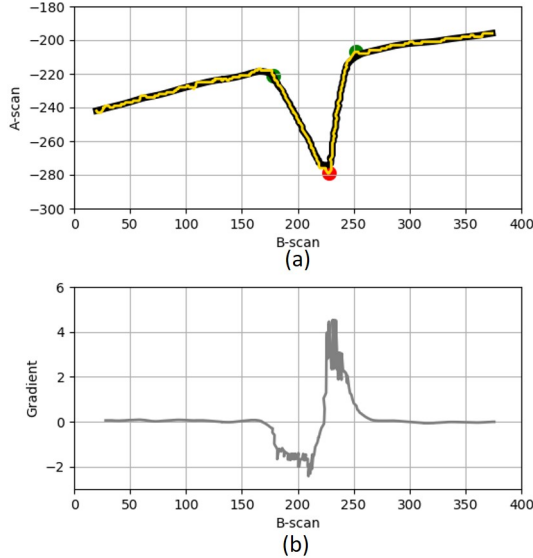


Fig. 6. Wound top layer detection and geometric analysis. (a) The AMAL detection result is shown in yellow while the de-noised result is shown in black. The estimated start and end of the wound are shown in green, while the deepest point is shown in red. (b) The gradient of the top layer of the wound after being de-noised.

using the adjusted mean arc length (AMAL) graph search method of Keller et al. [9] to find the top layer of the wound (Fig. 6a). Next, we rotate the top layer such that the non-wound portion is horizontal. We use a Gaussian 1D filter to denoise the top layer, and then calculate the gradient of the smoothed top layer. We define the start point as the first point from left to right where the gradient falls below a threshold. Similarly, we define the end point as the first point from right to left where the gradient exceeds a threshold. The point that has smallest position is the deepest point of the wound.

E. Suturing Path Planning

Once the wound is identified, we generate a suitable suturing path in the B-scan plane. We fix the suturing center to reduce the interaction forces between the needle and tissue compared to the moving center suturing approach. To avoid the dead space (Fig. 2a-b), the distance from the left bite point to the deepest point, and the distance from the deepest point to the right exit point should be equal.

According to standard suturing practice, the suturing depth should exceed 50% of the wound depth [4]. We therefore chose a target suturing depth of 80%, from which we can calculate the left bite point and the right exit point. Using the known needle radius, we obtain two solutions for the suture center corresponding to these points in the B-scan plane. One solution lies within the tissue whereas the other is above it. We reject the in-tissue solution because its suturing path does not have the right bite point and the left exit point and use the other solution for planning.

After we obtain the suturing center in 3D, we generate the robot's path in joint space. First, we choose three points in the needle frame (the needle tip P_{N_1} , the needle body P_{N_2} , and the needle tail P_{N_3} , every point is a 3×1 matrix). These three points determine the suturing needle position and orientation. Second, we uniformly interpolate needle tip P_{O_1} milestones along the suturing path in the OCT frame. Because the relationship between these three points is fixed, for each milestone, we calculate the corresponding P_{O_2} and P_{O_3} . Using T_{OCT} from the calibration process, we transfer the milestones from the OCT frame to the world frame (P_{W_1} , P_{W_2} and P_{W_3}). For each milestone on the suturing path, we use the relationship

$$\begin{bmatrix} P_{W_1} & P_{W_2} & P_{W_3} \\ 1 & 1 & 1 \end{bmatrix} = T_{EE} T_N \begin{bmatrix} P_{N_1} & P_{N_2} & P_{N_3} \\ 1 & 1 & 1 \end{bmatrix}. \quad (2)$$

Finally, we use the Klamp't [5] numerical inverse kinematics (IK) solver to compute the robot configuration from the T_{EE} of every milestone. For the first IK solution, the solver is seeded with the robot's current configuration. For the remainder, the solver's is seeded from the last solution. Collision detection is used to prevent the robot from colliding with the environment or itself.

IV. EXPERIMENTS AND RESULTS

A. Parameter Selection and Calibration Results

We evaluated our system in two materials: a silicone rubber tissue phantom (Your Design Medical; Brooklyn, NY) and porcine skin. Because the scope of this paper does not include needle grasping, we stopped the robot after each full insertion to detach the needle and pull the attached suture through the tract. This allows the tissue to relax to its rest deformation, although the tissue is not perfectly elastic and therefore may not relax completely. The suture path is then imaged using the OCT system.

We performed 14 suturing needle insertions (8 for tissue phantom and 6 for porcine skin). We adjusted the OCT scanner before each attempt to ensure that the wound was within its the field of view. Furthermore, in real surgical

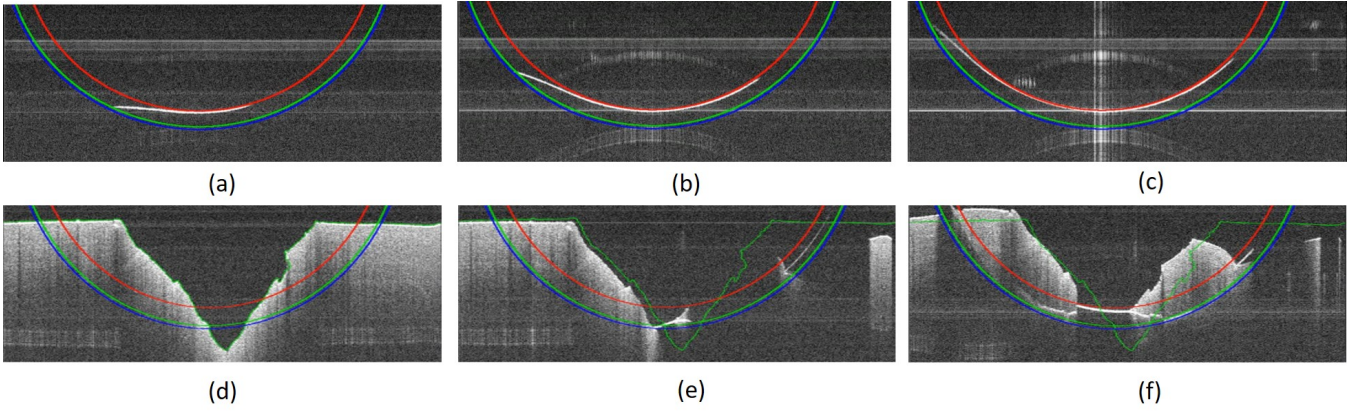


Fig. 7. Snapshots of the needle insertion process, showing the OCT B-scan data and the planned path for the needle, showing planned arcs for the inside face (red), needle tip (green), and outside face (blue). The jagged green line is the wound top layer in the undeformed state. In (a) – (c), the path is executed without the tissue phantom present, showing high accuracy of the calibration process. In (d) – (f), the needle is inserted into the tissue phantom, showing significant deformation. Note that OCT cannot see the needle outside face path because the laser cannot penetrate metal. The needle shadows the tissue, and also appears distorted in the tissue due to refraction.

settings, the needle will be grasped at a slightly different location every time. To simulate errors caused by grasping, we grasped the needle at the different location on the jaw for each insertion, such that transformations T_{OCT} and T_N changed. Notably, the wound shape varied across all 14 insertions. The wound width was 2.887 mm – 5.874 mm whereas the wound depth was 1.661 mm – 3.460 mm. The tissue surface was also not necessarily level with tilts of $\pm 8^\circ$ to simulate the real wound environment.

For calibration, we sampled 9 robot configurations to estimate the T_{OCT} and T_N . With these 9 robot configurations, the suturing needle was uniformly sampled in the OCT space with different positions and orientations (Fig. 8a), and we estimated T_{OCT} and T_N . The calibration performance from the target point cloud frame is shown in Fig 8b. Comparing the difference between T_{ICP}^{-1} and $T_{OCT}^{-1}T_{EE_i}T_N$ for our 14 groups of data, the translation RMSE was 0.114 mm – 0.263 mm, and the rotation RMSE was 0.012 rad – 0.038 rad.

To empirically tune and evaluate wound analysis, we gathered 590 B-scans of different size wounds, and compared our method against manual grading as ground truth. With the AMAL [9] parameter $x = 1.02$, AMAL detected all wound top layers successfully. The denoising Gaussian kernel standard deviation is set to be 8 pixels, and the gradient threshold to detect the start point of the wound and the end point of the wound is chosen to be -1.5 and $+1.5$, respectively. With these values, our methods successfully detected 582 wounds and keypoints compared to manual grading (98.6% success rate).

B. Needle Insertion Results

We first executed suturing paths in free space to visualize whether the needle follows our planned path. A representative result is shown in Fig. 7a-c, demonstrating close agreement. Next, we performed insertions in the tissue phantom (Fig. 7d-f). Because it is difficult to observe the suture path with OCT when the suture passes far below the

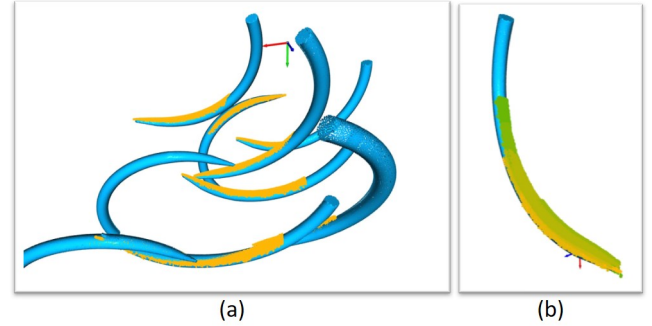


Fig. 8. Calibration results with 9 needle poses. (a) The source and target point clouds are drawn in yellow and blue, respectively. Each target point cloud is transformed using the estimated needle-robot pose and base calibration, showing a good fit. (b) Shown in the target point cloud frame, the source point clouds are drawn in different shades of yellow-to-green. The tip position estimates still have some residual error, whose magnitude is approximately half the width of the needle

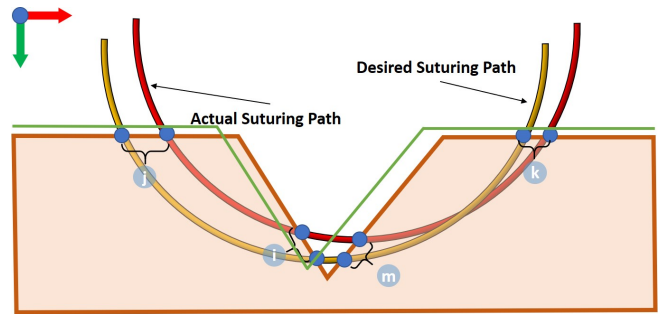


Fig. 9. The method used for suture grading. The tissue shape is after the needle pulled out, and the green line is the AMAL result before needle insertions. k) right bite point error. m) right exit point error. i) left bite point error. j) the left exit point error.

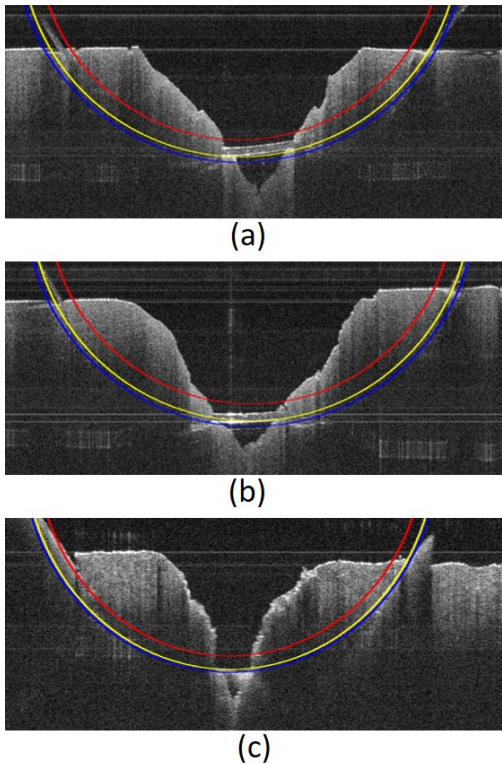


Fig. 10. OCT B-scan images of the sutures after the needle has passed through the tissue. (a) and (b) are in the tissue phantom, and (c) is porcine skin. The planned needle paths are shown for the needle inside face (red), outside face (blue), and suture top layer (yellow). Note: the shown B-scan may not be the same as the one in which planning occurred due to error in the C-scan direction.

TABLE I
TISSUE PHANTOMS SUTURE PERFORMANCE RMSE (UNIT:MM)

	B-scan (X)	A-scan (Y)	C-scan (Z)	3D
Right Bite	0.113	0.039	0.063	0.135
Right Exit	0.191	0.234	0.079	0.313
Left Bite	0.168	0.206	0.079	0.277
Left Exit	0.339	0.063	0.122	0.366
Total	0.219	0.160	0.089	0.286

tissue surface, we graded the accuracy of insertions by calculating the distance between the planned and actual points where the suture intersects the tissue (Fig. 9). However, due to tissue deformation, it is difficult to judge whether the needle bites and exits at our planned points. Therefore, we manually removed the needle from the needle driver, and pulled the suture through the wound. Because the friction from the needle is removed and the suture is loose, the wound will approximately return to its resting shape (Fig. 10). By inspection, the sutures' paths are in the planned boundary of the needle. The RMSE for each of the four grading points for the tissue phantom and porcine skin are shown in Tables I and II, respectively. The RMSE for each of the grade points and overall was lower than the needle width.

TABLE II
PORCINE SKINS SUTURE PERFORMANCE RMSE (UNIT:MM)

	B-scan (X)	A-scan (Y)	C-scan (Z)	3D
Right Bite	0.169	0.027	0.000	0.171
Right Exit	0.102	0.117	0.052	0.164
Left Bite	0.044	0.096	0.061	0.122
Left Exit	0.421	0.061	0.077	0.432
Total	0.233	0.083	0.055	0.254

V. CONCLUSION

We presented a method for OCT-guided calibration and path planning for a suturing needle to be guided autonomously and accurately through soft tissue. Calibration, wound detection, and path planning are all performed using the input from OCT imaging. Execution performance was graded by the observing the path followed by the suture, demonstrating sub-millimeter errors between the planned and executed entry and exit points, with error magnitude at approximately half the width of the needle.

In future research, we intend to address some remaining issues with this approach. First, the needle pose calibration error is approximately $20\times$ larger than the best-reported OCT-based needle calibration results in the literature, because the curved needle and needle grasping error introduce more challenging initialization and imaging conditions. It may also be possible to develop more advanced image processing techniques to address OCT imaging artifacts such as highlights, refraction, shadowing, and mirror images. Solving these issues is a prerequisite for real-time guidance during suturing. We are also interested in extending our work to the multi-throw case with regrasping.

REFERENCES

- [1] T. Alrasheed, J. Liu, M. M. Hanasono, C. E. Butler, and J. C. Selber. Robotic microsurgery: Validating an assessment tool and plotting the learning curve. *Plastic and reconstructive surgery*, 134(4):794–803, 2014.
- [2] P. Besl and N. McKay. A method for registration of 3-d shapes. *IEEE Transactions on Pattern Analysis and Machine Intelligence*, 14(2), 1992.
- [3] M. Draeos, B. Keller, G. Tang, A. Kuo, K. Hauser, and J. Izatt. Real-time image-guided cooperative robotic assist device for deep anterior lamellar keratoplasty. In *IEEE International Conference on Robotics and Automation (ICRA)*, 2018.
- [4] Ethicon. *Wound Closure Manual*. Ethicon Inc., 2005.
- [5] K. Hauser. Robust contact generation for robot simulation with unstructured meshes. In *International Symposium on Robotics Research*, 2013.
- [6] D. Huang, E. Swanson, C. Lin, J. Schuman, W. Stinson, W. Chang, M. Hee, T. Flotte, K. Gregory, C. Puliafito, and J. Fujimoto. Optical coherence tomography. *Science*, 254:1178–1181, 1991.
- [7] R. Jackson and M. Cavusoglu. Needle path planning for autonomous robotic surgical suturing. In *IEEE International Conference on Robotics and Automation (ICRA)*, 2013.
- [8] H. Kang and J. Wen. Autonomous suturing using minimally invasive surgical robots. In *IEEE International Conference on Control Applications*, 2000.
- [9] B. Keller, D. Cunefare, D. Grewal, T. Mahmoud, J. Izatt, and S. Farsiu. Length-adaptive graph search for automatic segmentation of pathological features in optical coherence tomography images. *Journal of Biomedical Optics*, 21(7):076015, 2016.

- [10] B. Keller, M. Draelos, G. Tang, S. Farsiu, A. Kuo, K. Hauser, and J. Izatt. Real-time corneal segmentation and 3d needle tracking in intrasurgical oct. *Biomedical Optics Express*, 9(6):2716–2732, 2018.
- [11] M. A. Nasser, M. Maier, and C. Lohmann. A targeted drug delivery platform for assisting retinal surgeons for treating age-related macular degeneration (amd). In *Int. Conf. IEEE Eng. Med. Biol. Soc. (EMBC)*, pages 4333–4338, 2017.
- [12] S. Pedram, P. Ferguson, J. Ma, E. Dutson, and J. Rosen. Autonomous suturing via surgical robot: An algorithm for optimal selection of needle diameter, shape, and path. In *IEEE International Conference on Robotics and Automation (ICRA)*, 2017.
- [13] S. Sen, A. Garg, D. G. ad S. McKinley, Y. Jen, and K. Goldberg. Automating multi-throw multilateral surgical suturing with a mechanical needle guide and sequential convex optimization. In *IEEE International Conference on Robotics and Automation (ICRA)*, 2016.
- [14] C. Staub, T. Osa, A. Knoll, and R. Bauernschmitt. Automation of tissue piercing using circular needles and vision guidance for computer aided laparoscopic surgery. In *IEEE International Conference on Robotics and Automation*, 2010.
- [15] H. Yu, J. Shen, R. Shah, N. Simaan, and K. Joos. Evaluation of microsurgical tasks with oct-guided and/or robot-assisted ophthalmic forceps. *Biomedical Optics Express*, 6(2):457–472, 2015.
- [16] M. Zhou, M. Hamad, J. Weiss, A. Eslami, K. Huang, M. Maier, C. Lohmann, N. Navab, A. Knoll, and M. A. Nasser. Towards robotic eye surgery: Marker-free online hand-eye calibration using optical coherence tomography images. *IEEE Robot. Autom. Lett.*, 3(4):3944–3951, 2018.
- [17] M. Zhou, X. Hao, A. Eslami, K. Huang, C. Cai, C. Lohmann, N. Navab, A. Knoll, and M. Nasser. 6dof pose estimation for robot-assisted vitreoretinal surgery. *IEEE Access*, 7:63113–63122, 2019.
- [18] Q. Zhou, J. Park, and V. Koltun. Open3d: A modern library for 3d data processing. *arXiv:1801.09847*, 2018.